Ocean Surface Albedo and Its Impact on Radiation Balance in Climate Models

J. LI, J. SCINOCCA, M. LAZARE, N. MCFARLANE, K. VON SALZEN, AND L. SOLHEIM

Canadian Centre for Climate Modelling and Analysis, Meteorological Service of Canada, Victoria, British Columbia, Canada

(Manuscript received 28 November 2005, in final form 27 April 2006)

ABSTRACT

An analysis of several ocean surface albedo (OSA) schemes is undertaken through offline comparisons and through application in the Canadian Centre for Climate Modelling and Analysis (CCCma) fourth-generation atmospheric general circulation model (AGCM4). In general, each scheme requires different input quantities to determine the OSA. Common to all schemes is a dependence on the solar zenith angle (SZA). A direct comparison of the SZA dependence of the schemes reveals significant differences in the predicted albedos. Other input quantities include wind speed and aerosol/cloud optical depth, which are also analyzed.

An offline one-dimensional radiative transfer model is used to quantitatively study the impact of ocean surface albedo on the radiative transfer process. It is found that, as a function of SZA and wind speed, the difference in reflected solar flux at the top of the atmosphere is in general agreement between OSA schemes that depend on these quantities, with a difference <10 W m^{-2}. However, for simpler schemes that depend only on SZA the difference in this flux can approach 10–20 W m^{-2}.

The impact of the different OSA schemes is assessed through multiyear simulations of present-day climate in AGCM4. Five-year means of the reflected clear-sky flux at the top of the atmosphere reveal local differences of up to several watts per meters squared between any of the schemes. Globally, all schemes display a similar negative bias relative to the Earth Radiation Budget Experiment (ERBE) observations. This negative bias is largely reduced by comparison with the recently released Clouds and the Earth's Radiant Energy System (CERES) data. It is shown that the local upward clear-sky flux at the surface is more sensitive to the OSA formulation than the clear-sky upward flux at the top of atmosphere. It is found that the global energy balance of the model at the top of the atmosphere and at the surface is surprisingly insensitive to which OSA scheme is employed.

1. Introduction

Solar radiation is the primary energy source for the atmospheric general circulation and the hydrological cycle. The coupling between an atmospheric general circulation model (AGCM) and an oceanic general circulation model (OGCM) depends strongly on the radiative energy flow through the earth–atmosphere system. For the radiative energy budget near the surface the shortwave solar energy accounts for most of the heat flux transferred to the ocean. The solar radiation transferred into the upper-ocean layers affects the stability of the ocean mixed layer and the sea surface temperature. Consequently, the oceanic surface albedo (OSA) plays a key role in determining the energy flow exchange between atmosphere and ocean and so is an important issue for the coupling of atmosphere and ocean models.

In the last several decades, several OSA schemes have been proposed based on observations and theoretical calculations. However, the analytic expressions and the dependent variables that comprise these schemes differ greatly. Some schemes depend only on the solar zenith angle (SZA) while others additionally depend on quantities like wind speed and/or cloud optical depth. Furthermore, most schemes are only valid for the broadband approximation (i.e., one albedo for all wavelengths of incident radiation) while others provide albedos for differing spectral bands. Some schemes distinguish between clear and cloudy conditions while others represent long time averages over both.

It is anticipated that this wide variety of OSA schemes will be associated with differing radiative impact. This is generally a complicated process. Effective tools for

Corresponding author address: Dr. Jiangnan Li, Canadian Centre for Climate Modelling and Analysis, Meteorological Service of Canada, P.O. Box 1700, University of Victoria, Victoria BC V8P 2Y2, Canada.
E-mail: Jiangnan.Li@ec.gc.ca

such study are the one-dimensional radiative transfer models by which the influence of OSA on the upward flux at the top of the atmosphere (TOA) and the solar energy flow at the surface can be analyzed. This "offline" tool provides a controlled way of highlighting differences in the radiative forcing associated with each OSA scheme. It also provides a basis for understanding the ultimate response of the climate system in fully interactive GCM climate integrations.

In this study we employ a combination of offline radiative transfer model calculations with integrations of the Canadian Centre for Climate Modelling and Analysis (CCCma) fourth-generation atmospheric general circulation model (AGCM4) to consider the impact of various OSA schemes on the climate system. In this "atmospheric" configuration AGCM4 is driven by prescribed sea surface temperatures and sea ice (this represents the first step in an attempt to gauge the impact of differing formulations of OSA that are currently in use). As well as intercomparing the schemes, each will be compared to observations—the Earth Radiation Budget Experiment (ERBE; Barkstrom 1984) and the recently released Cloud and the Earth's Radiation Energy System (CERES) data (Wielicki et al. 1998; the data are available online at http://asd-www.larc.nasa.gov/ceres/ASDceres.html). One of the motivating factors for this study is to determine the degree to which biases relative to these observations are sensitive to the OSA formulation employed.

The outline of the paper is as follows. In section 2 we will review the development of the OSA parameterization currently used in AGCM4 at CCCma. In this section we will also introduce three additional parameterizations of OSA, which will be considered in this study. In section 3, using a radiative transfer model, we perform offline comparisons of the different OSA schemes. In section 4 we present sensitivity experiments of present-day climate employing AGCM4. Finally in section 5 we conclude with a brief summary.

2. OSA parameterization

In this section we review the properties of the OSA parameterizations analyzed in the present study. We begin this discussion with a brief summary of the formulations employed by the CCCma.

a. CCCma operational OSA parameterizations

The CCCma second-generation atmospheric GCM (McFarlane et al. 1992), employed a relatively simple scheme for OSA, which depended on SZA and was independent of sky and surface wind conditions. The third-generation CCCma model, AGCM3 (McFarlane et al. 2005), employed the Hansen et al. (1983) fit to Cox and Munk's approximate theory (Cox and Munk 1954). This fit was both a function of SZA and wind speed. We shall refer to Hansen et al. (1983) as the H scheme. The H scheme fit to the Cox and Munk (CM) theory is illustrated in Fig. 1a where the albedo as a function of surface wind speed is plotted at five SZAs. Here the CM theory was plotted for light with a wavelength of 0.63 μm. As is clear from this plot, the H scheme fit tends to underestimate the albedo at all SZA and wind speeds. This was discussed by Barker and Li (1995). To correct this deficit Barker and Li simply adjusted the lead constant in the Hansen formulation, corresponding to a vertical shift or uniform increase, to enhance the albedo to more reasonable values.

In the AGCM4 the theory of Preisendorfer and Mobley (1986, hereafter PM86) is used to help formulate the OSA. The PM86 theory is more accurate than CM's approximation. For example, PM86 include the reflection for the diffused rays as well as the orientation of the wind relative to the incoming solar flux. In Fig. 1b we present the albedo predicted by PM86. At each SZA four curves are presented to represent the PM86 result: crosswind (blue lines) and along wind (red lines), and for each of these cases, single scattering (dashed lines) and multiple scattering (solid lines) albedos.

The parameterization used in AGCM4 is simply an approximate fit to the PM86 result. That is, no attempt was made to account for the orientation of the wind relative to the direction of the incoming solar flux. This is only an issue at large SZA. The specific form of this fit is presented in appendix A and is displayed in Fig. 1c. We shall refer to the fit to PM86 as the PM scheme. A comparison of the PM scheme to the H scheme used in AGCM3 is displayed in Fig. 1d. Here we see the PM parameterization increases the albedo relative to the H scheme in a way that is arguably more physical than simply increasing all values by a constant.

It is important to point out that the results of albedo presented in Fig. 1 are "direct beam" albedos. In addition to this direct beam, one must also include a "diffuse beam" contribution primarily due to photons that experienced at least one time scattering (Rayleigh, cloud, and aerosol scattering). One can define a diffuse albedo by integrating the direct beam albedo over all SZA with some suitable weighting (e.g., see PM86, their Fig. 21). In practice then, the albedo at any given time is simply the weighted sum of direct and diffuse albedo with the weighting depending on the fractions of downward direct and diffuse fluxes at the surface. However, to calculate these fractions requires a full radia-

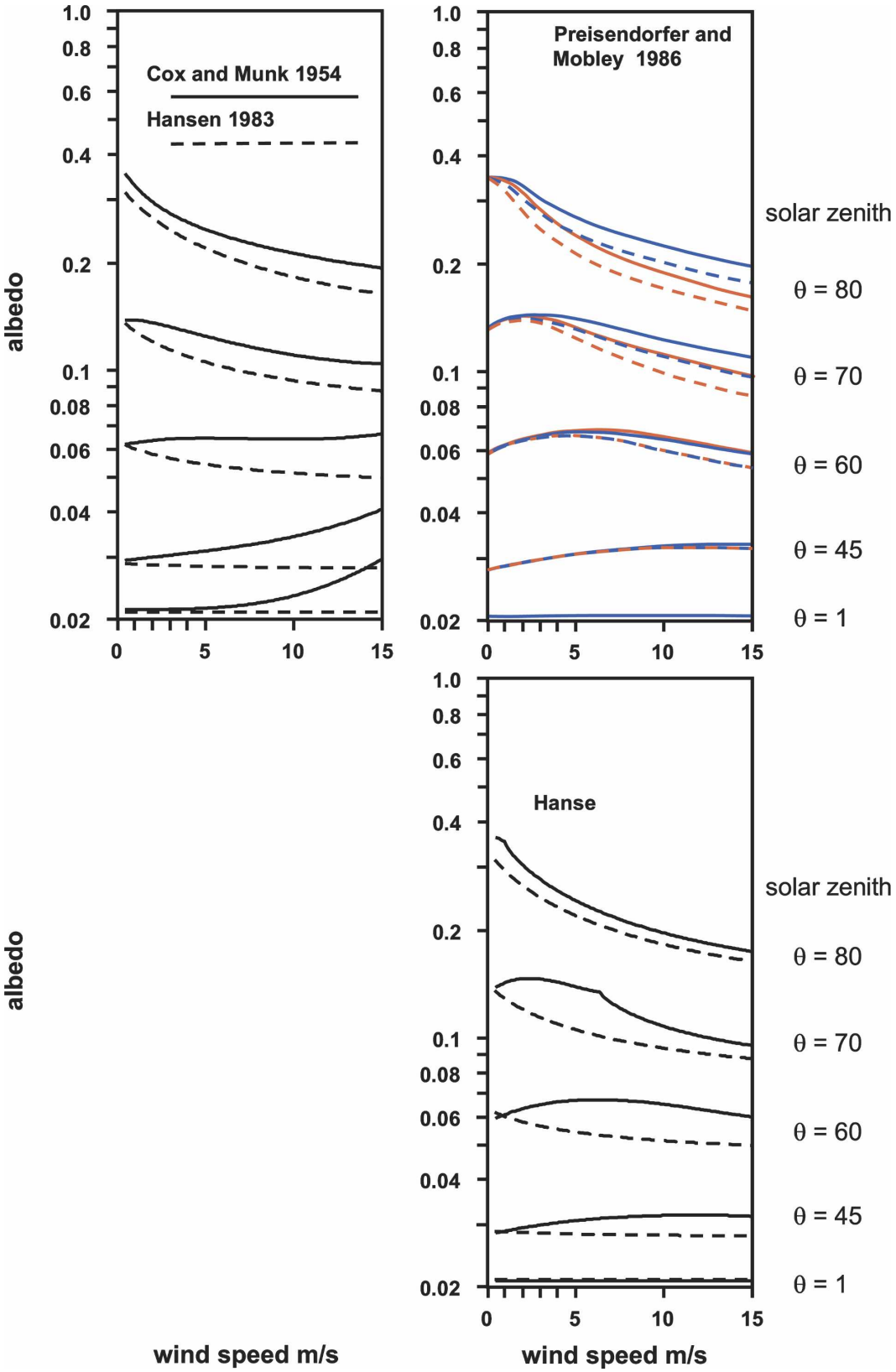

FIG. 1. (a) OSA against wind speed for five SZAs based on Cox and Munk (1954) and Hansen et al. (1983) (i.e., the H scheme). (b) The same as (a) but for PM86 with results for single scattering and multiple scattering, also across wind and along wind are separately accounted for. (c) Fitting PM86 to the PM scheme for the along-wind case. (d) Comparison of the results between the PM scheme (fitting results) and the H scheme.

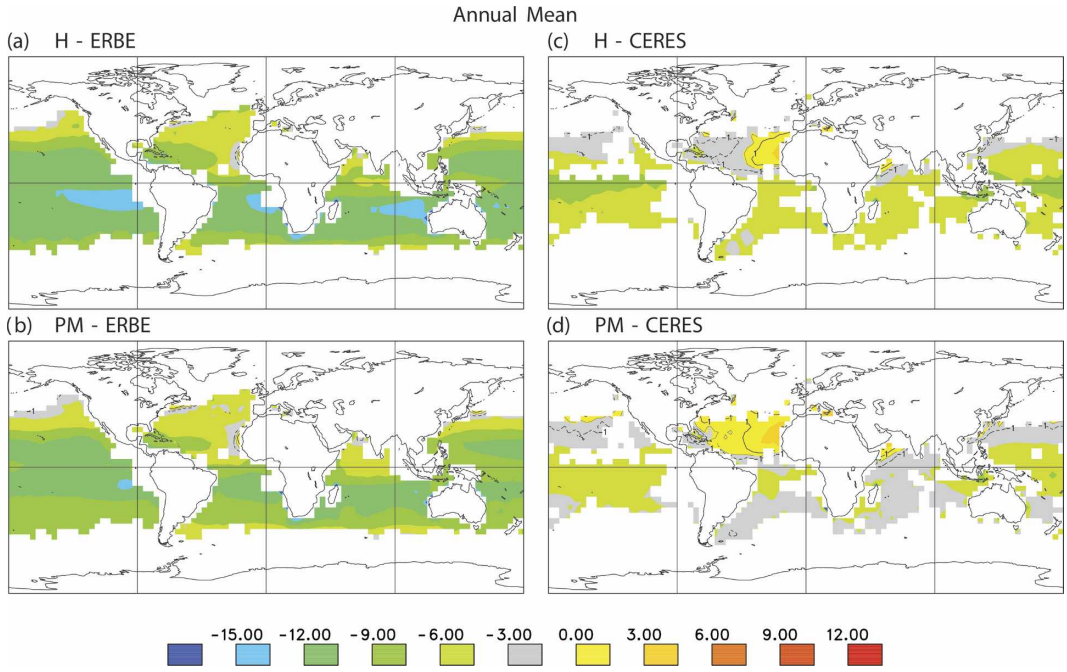

FIG. 2. (left) The GCM 5-yr annual mean upward solar flux at TOA against the ERBE data for the H and PM schemes (W m^{-2}). Only the region of valid ERBE data is accounted. (right) The same as (left), but for the GCM results against the CERES data.

tive calculation, which in turn requires the OSA. Therefore, in AGCM4, the OSA from the previous time step is used for the radiative transfer calculation at the current time step and this calculation is used to update the albedo for the next time step.

In the one-dimensional radiative transfer calculations, the direct- and diffuse-beam components are determined by a different procedure. There we first assume the fractions of surface downward direct and diffuse fluxes to obtain the albedo and then iterate the radiative transfer calculation to reach the final balance between the fractions of direct and diffuse fluxes.

Finally, AGCM4 employs an enhancement of OSA due to white caps. This modifies the albedos at relatively high wind speed (i.e., >15 m s^{-1}) and so does not significantly impact the albedos displayed in Fig. 1. The white cap formulation (Monahan and MacNiocaill 1986) is used for all OSA schemes employed in AGCM4 tested and described in appendix A.

As indicated in Figs. 1c,d, the PM parameterization represents a significant and realistic enhancement of the the OSA over that of Hansen et al. (1983). The use of the H scheme in both AGCM3 and AGCM4 is found to result in a significant negative bias in the upward radiative flux at the TOA relative to ERBE data (e.g., Barker and Li 1995). An interesting question is whether the enhanced albedos in the PM scheme significantly reduce this bias.

In Fig. 2 we present the the 5-yr mean of anomalous TOA upward clear-sky flux relative to ERBE from AGCM4 simulations (see section 4) employing the H (Fig. 2a) and PM (Fig. 2b) parameterizations of OSA. Figures 2a,b indicate that the negative bias with respect to ERBE is relatively insensitive to the enhancement in OSA offered by the PM parameterization. There occurs a significant qualitative similarity between patterns of the biases. Globally, the difference is greater than 8.5 W m^{-2} for the H scheme and roughly 7.5 W m^{-2} for the PM scheme. Locally, while the negative bias can exceed 12 W m^{-2} for both, these extremes cover a larger area for the H scheme. The ERBE estimate for clear-sky upward flux is consistently found to be higher than the modeled predictions (Loeb et al. 2003a,b).

Recently a 3-yr dataset of CERES was released (Wielicki et al. 1998). The mission of CERES is similar to the ERBE but with significant improvements in resolution and retrieval technology. In Figs. 2c,d we present the 5-yr mean of anomalous TOA upward clear-sky flux relative to CERES from AGCM4 simulations employing the H (Fig. 2c) and PM (Fig. 2d) schemes. Local biases relative to CERES are both positive and negative and of smaller magnitude than the biases relative to ERBE. The PM scheme seems to provide the estimate of the upward flux, which is closest to the CERES observations with local biases of less than ± 3 W m^{-2}. In the remainder of this paper we will compare the model

response to various OSA formulations against the CERES dataset. Biases relative to ERBE are generally large and negative and characterized by a structure similar to that in Figs. 2a,b.

b. Additional OSA parameterizations

In this section we briefly review three additional OSA schemes that will be investigated by the present study. The first two (Briegleb et al. 1986; Taylor et al. 1996) are simple in the sense that they depend solely on SZA. As such they represent time averages over other factors such as wind speed and direct versus diffuse conditions. The third scheme (Jin et al. 2002; the table data are available online at http://snowdog.larc.nasa.gov/jin/rtset.html; Jin et al. 2004) has an explicit dependence on wind speed in addition to SZA. Rather than depending on direct/diffuse conditions, this scheme has a dependence on the integrated aerosol/cloud optical depth to determine the fractional contributions from the direct and diffuse flux at the surface. Also, this scheme produces individual albedos for up to 24 solar bands rather than a single "broadband" albedo for the whole spectrum. Since none of these three schemes depends on the direct versus diffuse nature of the radiation they do not require the full radiative transfer calculation in order to determine the OSA.

The first scheme of Briegleb et al. (1986) represents a fit to the observations of Payne (1972). The form of the OSA is expressed as

$$A(\mu_0) = \frac{0.026}{1.1\mu_0^{1.7} + 0.065} + 0.15(\mu_0 - 0.1) \times (\mu_0 - 0.5)(\mu_0 - 1), \quad (1)$$

where $A(\mu_0)$ is the broadband OSA and μ_0 is the cosine of SZA (CSZA). Hereafter we shall refer to this formulation as the B scheme.

The second scheme of Taylor et al. (1996) represents a fit to 5 yr of observations compiled by aircraft measurements. The form of the OSA in this scheme is expressed as

$$A(\mu_0) = \frac{0.037}{1.1\mu_0^{1.4} + 0.15}. \quad (2)$$

Hereafter we shall refer to this formulation as the T scheme.

The solar zenith angle dependence of the B and T schemes is depicted in Fig. 3. This figure reveals that the B scheme produces a larger albedo than the T scheme at large SZA, θ_o. When the sun approaches the horizontal this difference can be as large as 0.15. At small values of SZA, the T scheme produces a larger albedo than the B scheme. This difference can be as much as 0.03. This indicates that the B scheme has a larger dynamic range than the T scheme.

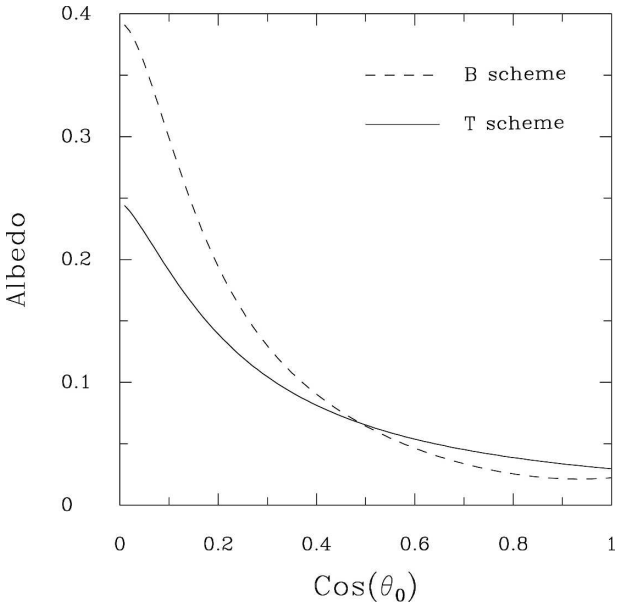

FIG. 3. Albedo vs cosine of SZA for the B and T schemes.

A comparison of the T and B schemes to the PM86 theory is provided in Figs. 4a,b, respectively. Since the T and B schemes depend only on SZA, their OSA values are constant with respect to wind speed and from Fig. 4 it would seem that the B scheme provides a reasonable fit to PM86. For the T scheme, however, the OSA appears to be systematically overpredicted at low SZA and underpredicted at large SZA relative to PM86.

The third scheme of Jin et al. (2002) derives its SZA and wind speed dependence from plane-parallel radiative transfer calculations that include the wind-blown roughened surface within the domain of the calculation. The surface is discretized by a set of inclined planes with random slopes that follow probability distributions given by Cox and Munk (1954). This scheme introduces an empirical dependence on aerosol/cloud optical depth to account for the effect of the direct and diffuse fluxes. Hereafter we shall refer to this formulation as the J scheme.

Generally, the larger the aerosol/cloud optical depth, the larger the fraction of the downward diffuse flux to the surface. A number of factors contribute to the aerosol/cloud optical depth. Aerosol concentrations are typically largest in the lower troposphere while the location of cloud varies from surface to tropopause. For example, one value of optical depth could correspond

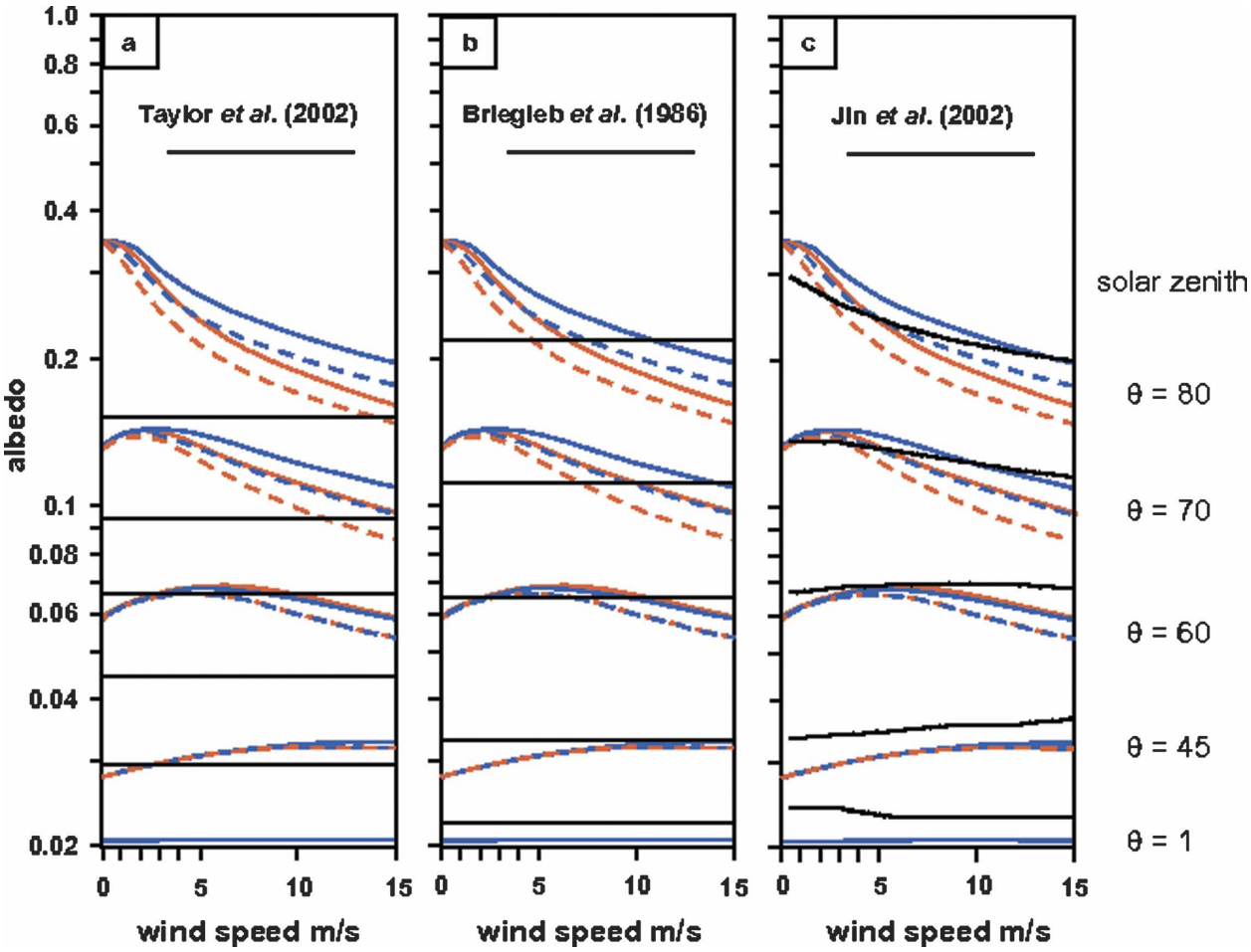

FIG. 4. The comparison of the B, T, and J schemes with the PM scheme. The color lines are the same as those in Fig. 1b. For the J scheme only the result of zero aerosol/cloud optical depth is considered.

to a variety of cloud and aerosol distributions. In principle the OSA will be sensitive to these different distributions since the fraction of direct relative to diffuse will be altered. In practice, however, test calculations indicate that this sensitivity has a small (roughly 5%) impact (Z. Jin 2003, personal communication).

In Fig. 4c the SZA and wind speed dependence of the OSA for the J scheme (averaged over all bands) relative to the PM86 theory is presented. For the comparison we have selected aerosol/cloud optical depth of zero for the J scheme. Consequently, this OSA estimate from the J scheme contains a small diffuse component associated with Rayleigh scattering. The J scheme is in close agreement with the PM86 theory at large SZA. At smaller SZA the J scheme provides a larger OSA relative to PM86. This difference, however, is larger than the expected enhancement of the J scheme due to Rayleigh scattering. Figure 4c also indicates that the dependence of the OSA on wind speed in the J scheme is generally weaker than PM theory. Both of these effects are consistent with the fact that the J scheme (and also the B and T schemes) includes bulk ocean scattering (i.e., contribution to backscattering from below the surface) while PM considers only reflectance from the surface (i.e., Fresnel).

It is interesting to note that the J and B schemes display an striking similarity in both their wind speed and SZA dependence (Figs. 4b,c). The B scheme is based on the observations from sea platforms. The J scheme is mostly from theoretical calculation but also adjusted with observations from similar sea platforms. It is anticipated, therefore, that the results of the B and J schemes might be quite similar and that any differences should be due to the additional input quantities that the J scheme depends upon (i.e., optical depth, wavelength, etc.).

In Fig. 5 we present the OSA dependence of the J scheme on the aerosol/cloud optical depth as a function

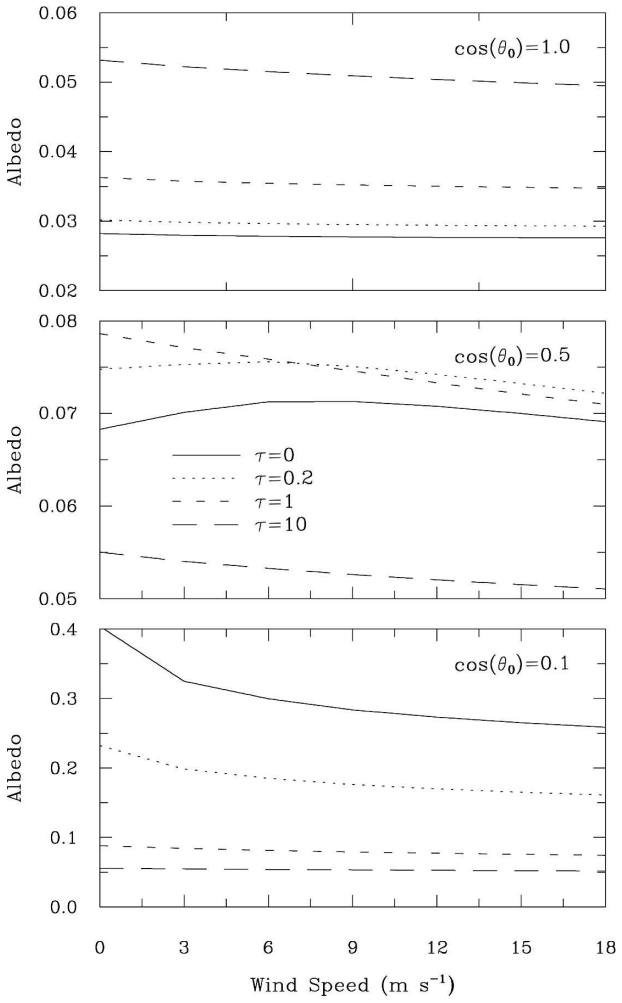

FIG. 5. Wind speed dependence of albedo for the J scheme as for different values of aerosol/cloud optical depth τ.

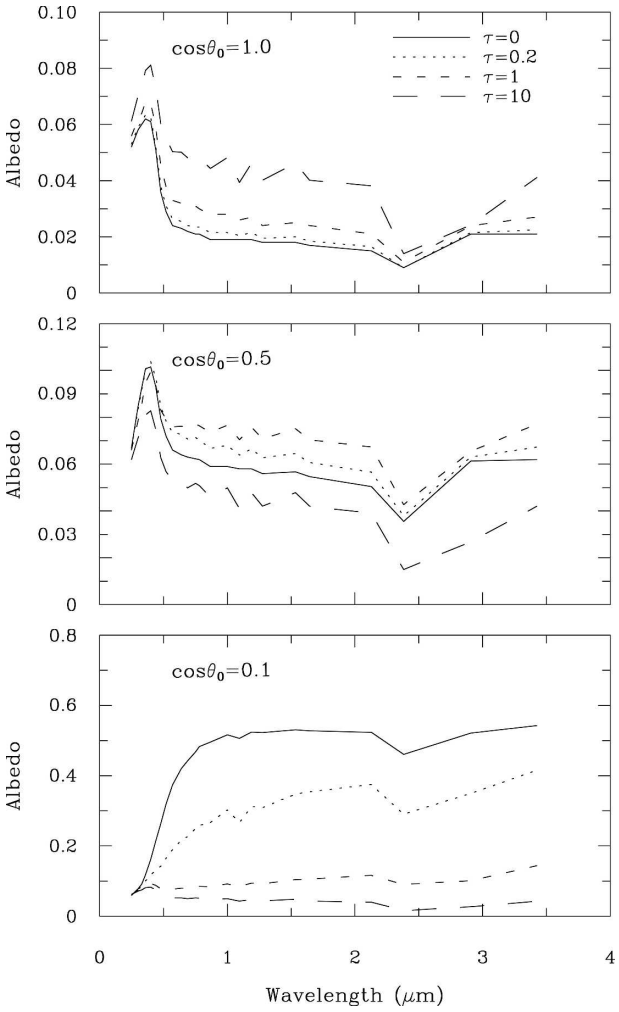

FIG. 6. For the J scheme, the spectral dependence of albedo for different values of aerosol/cloud optical depth τ. The wind speed is zero.

of wind speed at several SZAs. At large SZA (small CSZA), the albedo decreases with increasing optical depth while at small SZA (large CSZA), the albedo increases with increasing optical depth. This is consistent with the diffuse albedo having a larger value than the direct-beam albedo at small SZA and a smaller value at large SZA.

As indicated earlier, the J scheme allows for a spectral dependence of OSA. Since there occurs a significant spectral dependence of the solar incoming energy, and atmospheric absorption is highly spectral dependent, a spectral-dependent albedo has the potential to significantly impact the net radiative transfer in the atmosphere. In Fig. 6 we show the spectral variation of OSA for three different solar zenith angles and various optical depths. This figure indicates that there can be significant variation of the OSA with the wavelength of the incident radiation. For example, when the solar zenith angle is zero (i.e., the sun overhead), there is a sharp peak of ocean albedo at a wavelength of 0.4 μm, which corresponds to the color blue. Also Fig. 6 indicates that the relative height of this peak reduces as the aerosol/cloud optical depth increases, suggesting that a clearer sky implies a bluer ocean.

Another feature of the J scheme is that it allows for a dependence of the albedo on chlorophyll (e.g., Fig. 10 in Jin et al. 2002). In this study we have chosen not to investigate this dependence and so have specified a zero value of chlorophyll in all applications of the J scheme.

3. OSA radiative effects in a 1D radiative transfer model

To quantify the radiative impact of each OSA scheme we use a one-dimensional radiative transfer model.

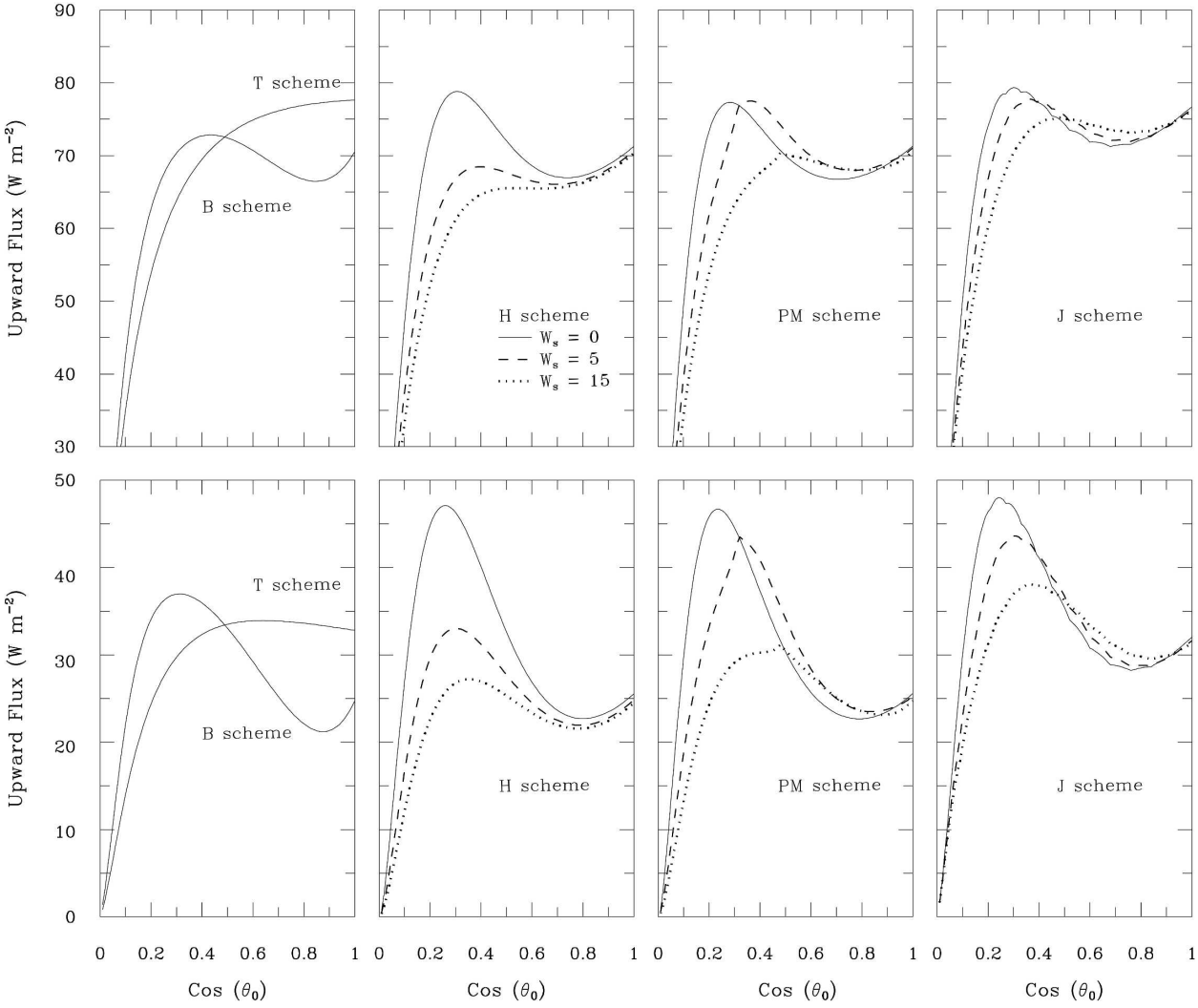

FIG. 7. Upward flux vs cosine of SZA for five OSA schemes. The results at (top) TOA and (bottom) at the surface. The aerosol/cloud optical depth is zero, W_s (m s^{-1}).

This allows us to compare the reflected solar flux at the TOA, the solar energy balance at the surface, and the change of aerosol/cloud forcing. The radiation algorithm of AGCM4 (Li and Barker 2005) is used here. This algorithm employs the correlated-k distribution method for gaseous transmission by resolving the spectrum from 2500 to 50 000 cm^{-1} into 31 intervals in cumulative probability function space. Aerosol and cloud optical properties are resolved into four bands of 0.2–0.69, 0.69–1.19, 1.19–2.38, and 2.38–4 μm, which is the same as the four-band spectral structure of the J scheme. The radiative transfer model was assessed by embedding synthetic cloud forms into a standard atmospheric profile (McClatchey et al. 1972).

The top row of Fig. 7 shows the reflected solar upward fluxes at the TOA corresponding to the different OSA schemes. The aerosol/cloud optical depth is set to zero. From Fig. 7 it can be seen that the B, H, PM, and J schemes display a reflected flux with both a maximum and minimum at roughly similar CSZA (~0.3 and 0.7, respectively). These appear to be the most pronounced for the zero wind speed case in the H scheme. These features arise from the fact that, as a function of SZA, the OSA and the incoming solar flux are nonlinear and of opposite tendency. For decreasing SZA (increasing CSZA) the incoming solar flux increases from a value of zero at SZA = 90° while the OSA generally decreases (i.e., see Figs. 1 and 3–6). At small SZA, this dependence is further influenced by decreased diffusion of the incoming radiation by clouds and aerosols. All schemes except the T scheme display this qualitative behavior of the upward fluxes. Although the B, H,

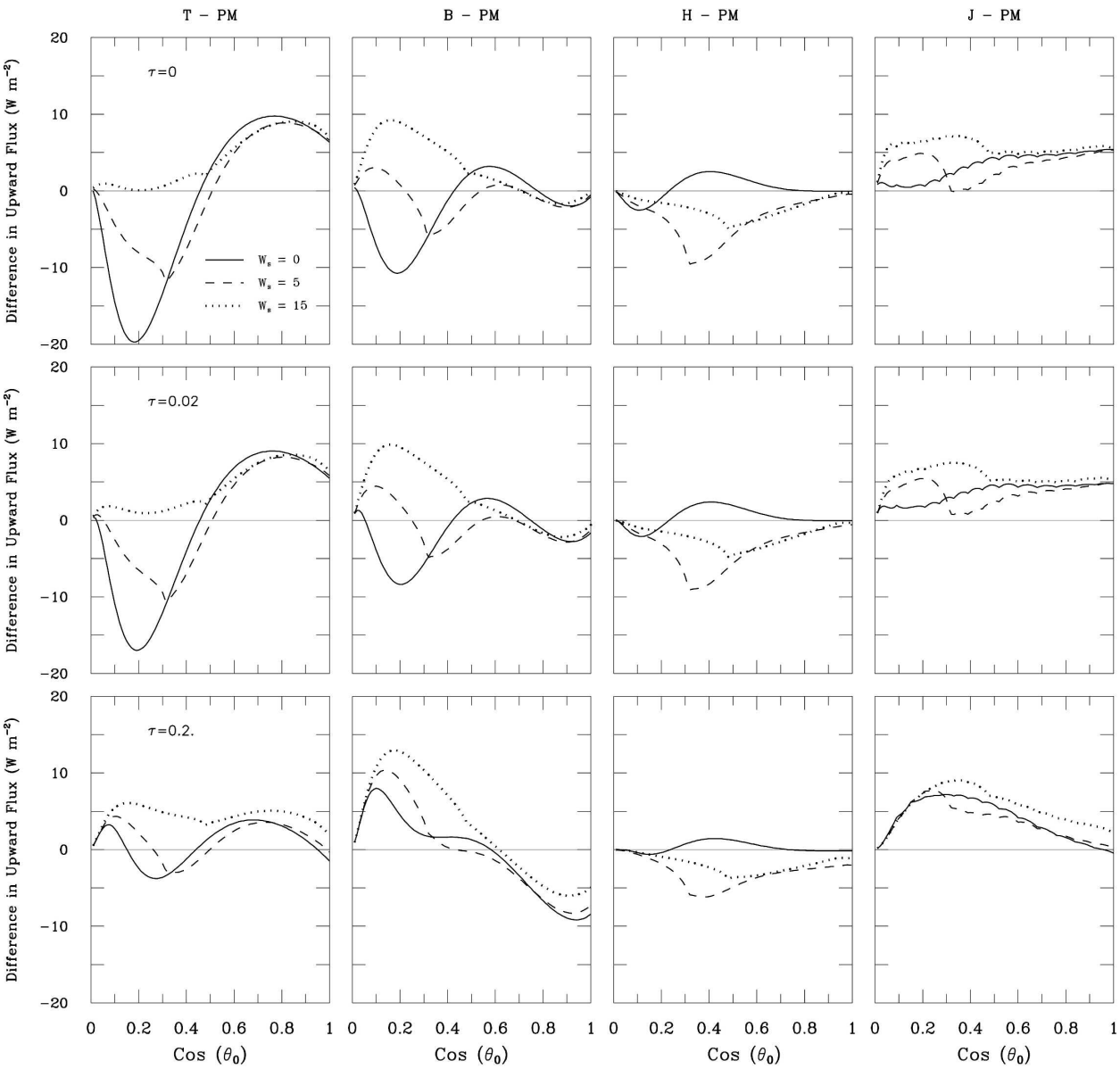

FIG. 8. The difference in upward flux at TOA. H − PM (J − PM, B − PM, and T − PM) refers to the results of the H (J, B, and T) scheme minus the results of the PM scheme, respectively. Here τ is the mean aerosol optical depth for the visible band. (top) τ = 0, (middle) τ = 0.02, and (bottom) τ = 0.2, W_s (m s^{-1}).

PM, and J schemes have similar structure in Fig. 7, there are quantitative differences, which can be as large as 10 W m^{-2}. The dependence on wind speed, also displayed in Fig. 7, reveals further quantitative differences between the H, PM, and J schemes.

In the bottom row of Fig. 7, the upward flux at the surface for the five schemes is displayed. A comparison of the top and bottom rows in Fig. 7 reveals that the difference in upward flux at the TOA corresponding to different wind speed is smaller than the same feature at the surface. Also the difference among the different schemes is reduced at TOA compared to at the surface. The reduction in difference is primarily due to Rayleigh scattering of the upward flux between the surface and the TOA.

The difference in the upward flux at the TOA for each of the schemes relative to the default PM scheme of AGCM4 is presented in Fig. 8. Cases corresponding to nonzero aerosol optical depth of increasing magnitude are displayed in the second and third row, respectively. The type of aerosol considered here is sea salt. According to Jacobson (2001) the global mean column

loading of sea salt is about 0.04 g m^{-2}. Two modes of sea salt are considered with effective radius of 1.75 μm for the coarse mode and 0.209 μm for the accumulation mode. It is assumed that 95% of sea salt is in the coarse mode and 5% is in the accumulation mode. The vertical distribution of sea salt is assumed to follow an exponential decay with a decay length of 200 m for the coarse mode and 500 m for the accumulation mode. The sea salt particle is hygroscopic as the particle size depends on relative humidity. The method of optical property parameterization for sea salt is based on Li et al. (2001) and Dobbie et al. (2003). We set the sea salt column loading as 0.044 g m^{-2}, which leads to the aerosol optical depth at visible band to be about 0.02 (second row). We also consider a larger case of sea salt column loading of 0.44 g m^{-2}, which corresponds to the aerosol optical depth at the visible band of about 0.2 (third row).

A comparison of the H and PM schemes (third column H − PM, second row) reveals that the upward flux for H is generally larger than for PM at zero wind speed. At nonzero wind speed the upward flux for H is generally smaller than that for PM. This is consistent with the behavior of the albedos displayed in Fig. 1d. A similar comparison of the upward flux for the J scheme to the PM scheme (fourth column J − PM) reveals that the J scheme is generally larger for all wind speeds. This is again consistent with the behavior of the albedos in these two schemes as illustrated in Fig. 4c (noting that the upward flux is impacted the least by large SZA). The difference between J and PM gets even larger for larger optical depth (second and third rows).

It is found that the differences in the upward flux at the surface among the five schemes are larger than the corresponding differences at the TOA. The difference could be over 20 W m^{-2}. We do not show the results of four other schemes against PM here, but the similar results of upward flux at the surface (with no aerosol) for all five schemes have been demonstrated in the bottom panels of Fig. 7. The downward flux at the surface is also affected by the OSA of diffuse light reaching the surface. However, the relative influence of diffuse light is small and cannot account for the larger differences found in upward flux at the surface.

In Figs. 6, 7, and 8, some results of the J scheme show small bumps in some lines that are mostly due to the linear interpolation from the tabulated numbers.

The 1D radiative transfer code was used to construct daily averaged values of the clear-sky upward flux at the TOA as a function of latitude. These are displayed in Fig. 9 for 15 January [i.e., corresponding to the midpoint of the December–February (DJF) season]. In appendix B, the method for evaluating daily averaged fluxes is discussed. Three wind speeds are considered. The aerosol loading is the same as in Fig. 8 with a sea salt loading of 0.04 g m^{-2} ($\tau \approx 0.02$ for the visible band). The calculation of the daily average in a one-dimensional radiation model is similar to that in GCM, but the regional variations of wind speed, atmospheric profile, aerosol loading, etc., could not be addressed. The differences among the different schemes decrease in the seasonally averaged results in comparison with those in Fig. 8. Generally the differences are less than 5 W m^{-2} in the middle and low latitudes.

For the upward flux at TOA, the J and T schemes are very close between latitudes of −45° and 30°, especially for wind speeds of 15 m s^{-1}. This is at first sight surprising. From the discussion of Fig. 4 it was anticipated that the B and J schemes should be most similar to each other. Relative to the J scheme the OSA in the T scheme was found to have a significant positive bias at low SZA and a significant negative bias at large SZA. Further analysis indicates that these oppositely signed biases relative to the J scheme almost completely cancel each other out in the daily average over SZA. It is this cancellation that is responsible for the similarity of the J and T schemes in Fig. 9. While the B scheme is most similar to the J scheme in Fig. 4, careful inspection reveals that its OSA is systematically smaller than the OSA of the J scheme. The daily average then results in an upward flux for the B scheme that is everywhere lower than the J scheme.

For zero wind speed the results of the H and PM schemes are very close, but then differ for nonzero wind speeds. As mentioned earlier, the H scheme is most sensitive to wind speed. Generally in tropical regions the B scheme is closest to the PM scheme. We will further discuss Fig. 9 in the context of the GCM results of the next section.

As discussed earlier, the J scheme provides albedos for 24 individual radiation bands. Up to this point we have considered the broadband albedo from the J scheme. That is, a band-averaged albedo. Here we shall consider the dependence of the OSA on the wavelength of the radiation for the four radiation bands employed in AGCM4. In Fig. 10 we plot the differences in the net flux at TOA and the surface between each of the four bands and the broadband value.

From Fig. 10 we can see that band 1 (visible range) of the four-band scheme produces lower net fluxes at TOA for large solar zenith angles and higher net fluxes at TOA for small SZAs. From Fig. 6, it can be seen that the albedo is higher in the visible range compared to the spectral mean results. As the SZA increases the difference reduces and at very large SZA the albedo in

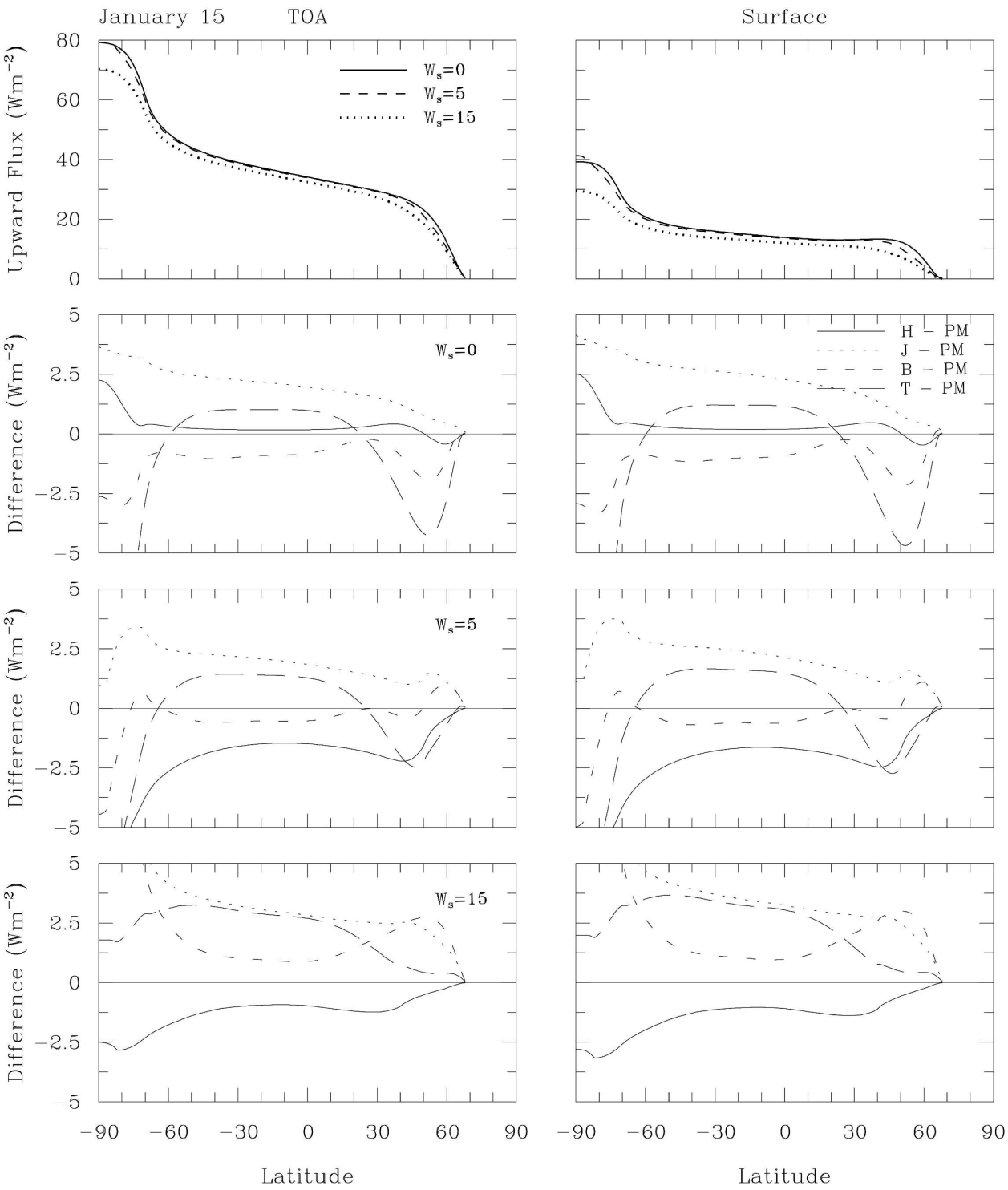

FIG. 9. (top) The latitudinal dependent daily mean upward fluxes at TOA and surface for the PM scheme. (bottom) The difference between other schemes to the PM scheme. H − PM (J − PM, B − PM, and T − PM) refers the results of H (J, B, and T) scheme minus the results of the PM scheme, respectively. Different wind speeds of (second row) zero, (third row) 5 m s^{-1}, and (fourth row) 15 m s^{-1} are considered.

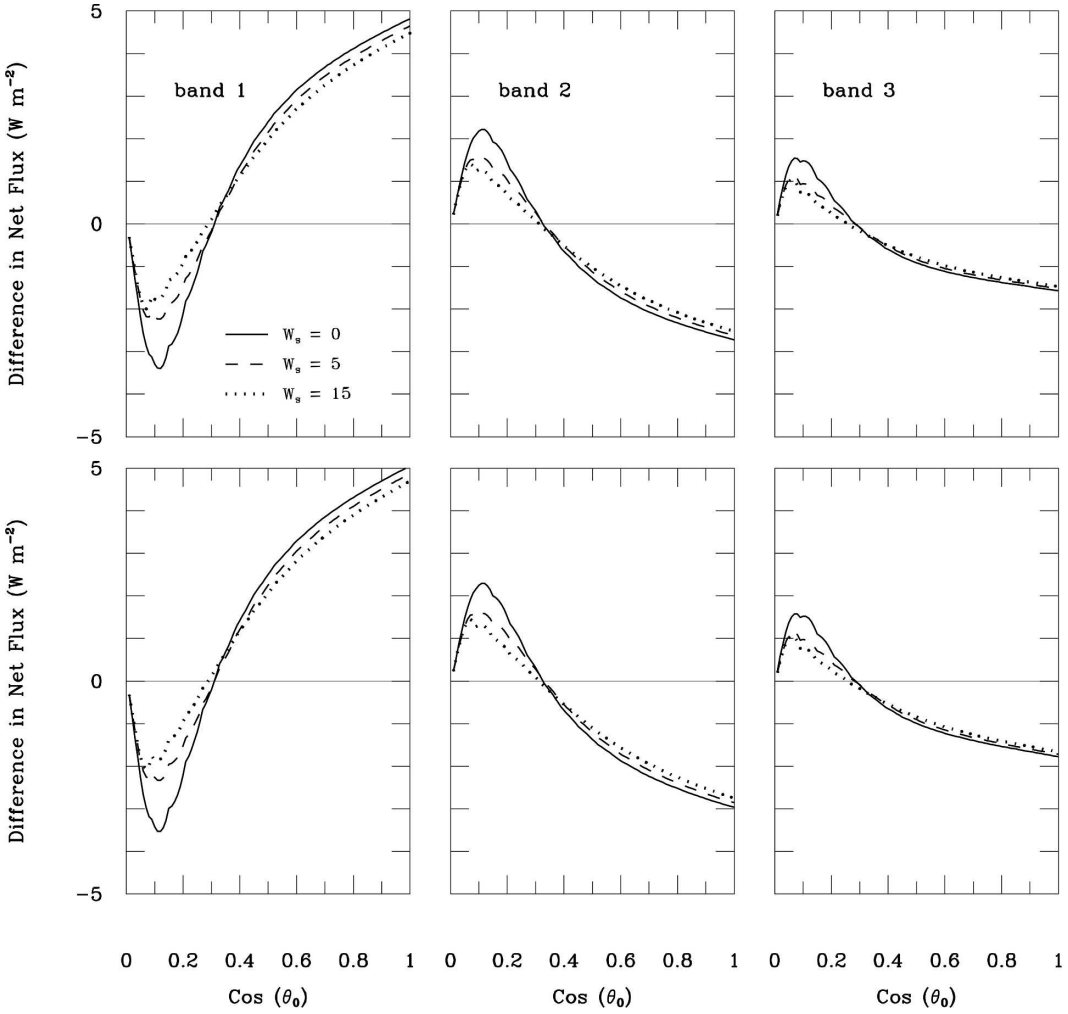

FIG. 10. The differences in the net flux at TOA and surface as for the four-band spectral J scheme minus the broadband J scheme, W_s (m s^{-1}).

the visible range becomes smaller in comparison with other spectral ranges. The results for bands 2 and 3 are opposite to that for band 1. The results for band 4 have not been shown since these are much smaller in magnitude (i.e., differences of <0.5 W m^{-2}).

The net flux integrated over the four bands of the four-band J scheme is very similar to the net flux of J broadband scheme, with difference <0.2 W m^{-2} in flux. Also there is almost no noticeable difference in the heating rate. Thus, the total radiative flux and heating rate are not strongly dependent on the spectral dependence of the OSA. However, climate models may also include chemical and biological process for which the radiative flux at a certain specified ranges, such as the ultraviolet (UV) and photosynthetic active radiation (PAR), are required. For these processes it is anticipated that the spectral dependence of the OSA will be more important.

Finally we study the influence of OSA on the aerosol/cloud forcing. The forcing refers to the difference in flux of two calculations with and without aerosol/cloud. Figure 11 shows the aerosol forcing at TOA for the five schemes. Once again, a sea salt column loading of 0.04 g m^{-2} is employed (as in Fig. 8). While it was found that upward fluxes at the TOA differed significantly between the B and T schemes (i.e., Figs. 7 and 8), Fig. 11 indicates that the aerosol forcing for these two schemes is very similar. This may be understood as follows: the B and T schemes do not directly depend on optical depth. The added aerosol optical depth, therefore, represents only a small perturbation to the gaseous optical depth. Consequently, the perturbation impact on the upward flux will be approximately linear in the optical depth perturbation (Li and Min 2002) resulting in only modest differences. Note that the forcing becomes positive for small SZA. This is because at a small SZA, the

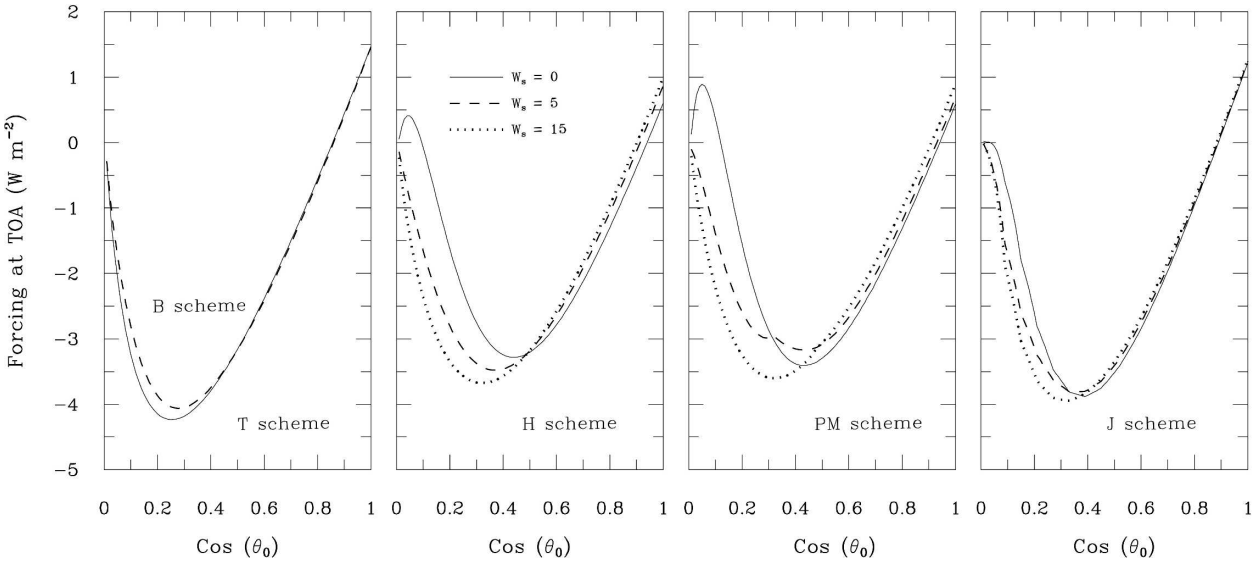

FIG. 11. Aerosol forcing at TOA for five schemes, W_s (m s^{-1}).

forward scattering is enhanced for existing aerosol particles and this leads to less reflectance at TOA.

Again it is shown in Fig. 11 that the H and PM schemes are more sensitive to wind speed in aerosol forcing in comparison with the J scheme. The J scheme is more similar to the B and T schemes in this regard. Figure 11 shows that the aerosol/cloud forcing generally increases with increasing wind. This can be understood as follows: when aerosols exist, the downward solar photons have a higher probability of scattering, especially for large solar zenith angles. Hence, less solar flux reaches the surface, and the role of surface albedo decreases and wind speed dependence decreases. Therefore the difference in upward flux with and without aerosol could be larger for a larger wind speed. Thus, the forcing of aerosol largely increases in the larger wind speed case.

We do not show the relation between all-sky forcing and OSA. The cloud optical depth is usually larger than 1, a large amount of solar energy is reflected back. The surface albedo has limited impact on this part of the flux.

4. GCM simulations

In this section we will characterize the impact of the various OSA schemes, on the climate by performing present-day climate simulations with the AGCM4. This model employs a spectral resolution of T47 with 35 vertical levels that monotonically increase from 100 m at the surface to up to 1 mb. AGCM4 is based on the third-generation CCCma AGCM (McFarlane et al. 2005) with the following additions/modifications: a new shallow-convection scheme (von Salzen and McFarlane 2002; von Salzen et al. 2005), a new prognostic cloud scheme based on the cloud microphysical processes of Lohmann and Roeckner (1996), a new correlated-*k* distribution radiation scheme (Li and Barker 2005), and a bulk aerosol parameterization of sea salt, sulfate, and dust with optical properties parameterized based on Li et al. (2001), Li and Min (2002), and Dobbie et al. (2003). In all GCM simulations, a parameterization of the influence of white caps on the OSA (Monahan and MacNiocaill 1986) has been employed (see appendix A).

The model is forced by a repeated annual cycle of sea surface temperatures and sea ice extent corresponding to an ensemble averaged over the Second Atmospheric Model Intercomparison Project (AMIPII) period (Gleckler 1996). In the following analysis 5-yr climate integrations are performed with each OSA scheme and the results are ensemble averaged to reduce the impact of natural variability.

In Fig. 12 the 5-yr mean, seasonal mean, June–August (JJA), and DJF OSA for each scheme are displayed. On the top right of each panel we have also indicated the globally integrated OSA in each of these seasons. Here the OSA has been calculated as the ratio of the broadband upward solar flux to the downward solar flux at the ocean surface. This diagnostic method allows the results for broadband OSA schemes and the multiple-band OSA scheme (i.e., the J scheme) to be directly compared.

A number of the differences evident in Fig. 12 are consistent with the offline analysis of the previous two sections. For example, from Fig. 3 it was found that,

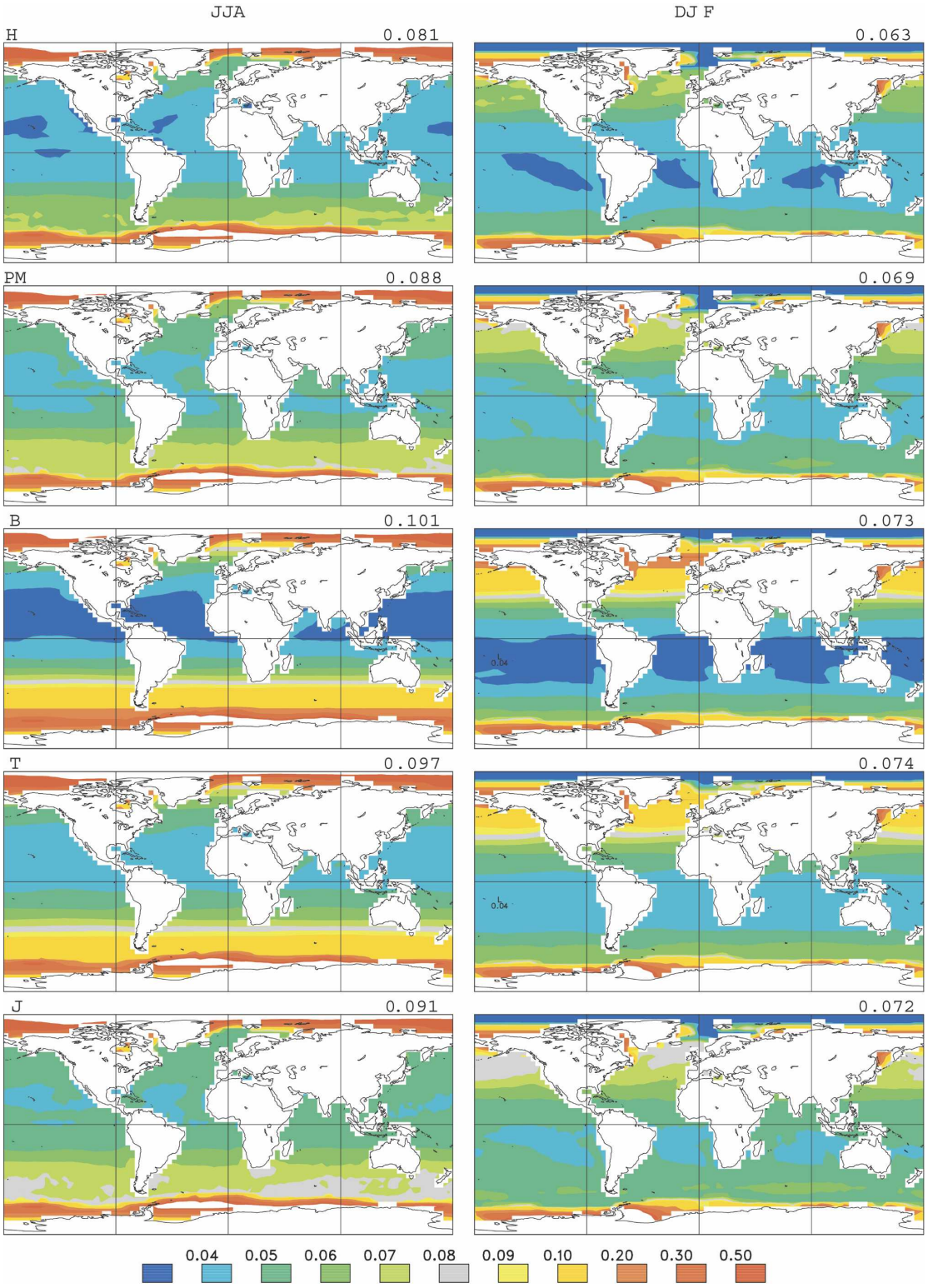

FIG. 12. GCM 5-yr mean surface albedo for the five schemes. The results for (left) JJA and (right) DJF. The numbers shown at top of each panel are the oceanic global mean value.

relative to the T scheme, the B scheme had a larger albedo at large SZA and a smaller albedo at small SZA. This is evident in Fig. 12 when the B and T schemes are compared in the Tropics and extratropics (i.e., low and high SZA, respectively). Since the B and T schemes depend only on SZA, it was anticipated that they should have less structure than the H, PM, and J schemes, which depend on a number of additional factors. This is also apparent in Fig. 12.

Of the H, PM, and J schemes, Figs. 1 and 4 suggest that the H scheme should produce the smallest OSA. This is also apparent in Fig. 12. Note also that the globally integrated OSA in both JJA and DJF is significantly lower in the H scheme relative to the PM and J schemes. A comparison of the globally integrated OSA between the PM and J schemes indicates that the J scheme produces a slightly larger albedo for each season. This result was not as obvious from offline calculations.

Since the global distribution of OSA is not a observable quantity, we employ comparisons of the observed versus modeled clear-sky upward flux at the TOA to evaluate the OSA schemes. In Fig. 13 the 5-yr mean TOA clear-sky reflected upward flux of the five schemes are plotted as anomalies away from the recent observation data of CERES. In regions where CERES data are missing (e.g., the coastal region near South America), clouds always appeared and clear-sky observations could not be performed. In these regions no anomalies are plotted. Also such regions are not included in calculating the global mean values. Global mean values are plotted at the top right of each panel (with CERES estimates in parentheses).

Figure 13 shows that the GCM results of upward flux at TOA are close to those of CERES with local biases of less than ± 6 W m^{-2} in most of regions. The worst case is the H scheme in DJF in which local biases of over -9 W m^{-2} appears for a lot of areas in Tropics and southern subtropical regions. In JJA the T scheme is closest to the CERES data while in DJF the J scheme is closest to the CERES data.

Closer scrutiny of Fig. 13 indicates more subtle similarities and differences in the model response to each of the OSA schemes. For example, in DJF (second column) all schemes display a north–south dipole pattern of the TOA upward flux about the equator. North of the equator the bias relative to CERES is positive while south of the equator the bias is negative. In JJA, the pattern of anomalies for all schemes seems to switch to an east–west dipole pattern with negative anomalies over the Pacific Ocean.

Figure 13 also indicates a strong similarity in the pattern of upward flux at the TOA between the T and J schemes. This similarity is anticipated from the daily average comparisons displayed in Fig. 9. However, there it was found that integration over the diurnal cycle resulted in the cancellation of large differences between the OSA of the T and J schemes.

In addition to the OSA, the clear-sky upward flux relies on aerosol distribution, its loading, and Rayleigh scattering. For example in the northern Atlantic, most of the OSA schemes produce the higher upward flux at TOA compared to the CERES. This probably is due to the high aerosol loading produced by GCM in this region. Because of these multiple factors it is not possible to identify which OSA scheme most closely matches observations.

In Fig. 14 the upward solar fluxes at the ocean surface are shown for the five different schemes. General trends predicted from the daily average fluxes of Fig. 9 are observed in the GCM response. For example, the H scheme generally produces the smallest flux while the J scheme produces the largest flux. As discussed earlier, Fig. 9 also predicts that there should be a close similarity between the T and J schemes at the surface and at the TOA in the Tropics and subtropics. While the TOA fluxes in Fig. 13 seemed to validate this prediction, the surface fluxes in Fig. 14 do not. The reason for this is not obvious. It is important to note, however, that in the offline calculations of Fig. 9 the atmospheric profile, wind speed, and aerosol distribution are fixed and there is no climatic feedback. This may have a larger impact on the surface response than the TOA response.

The globally integrated energy balance in the GCM experiments for each of the OSA parameterizations provides a sensitive measure of the model response to each scheme. Averaged over the 5-yr experiment the control run employing the PM scheme produced a net energy balance of 0.375 W m^{-2} at the surface (ocean only) and 0.332 W m^{-2} at the top of the atmosphere. While differences in clear-sky flux at the surface and the TOA have been identified between climates employing each of the OSA formulations, the net energy balance is found to be relatively insensitive. The use of either the H, T, B, or the J scheme produces energy balances that are generally within 1 W m^{-2} at the oceanic surface and at the TOA. From this we conclude that, as expected, OSA has only a modest impact on the response of the model when all-sky conditions are considered.

5. Conclusions

The surface radiation budget has long been recognized as fundamental to understand the climate system

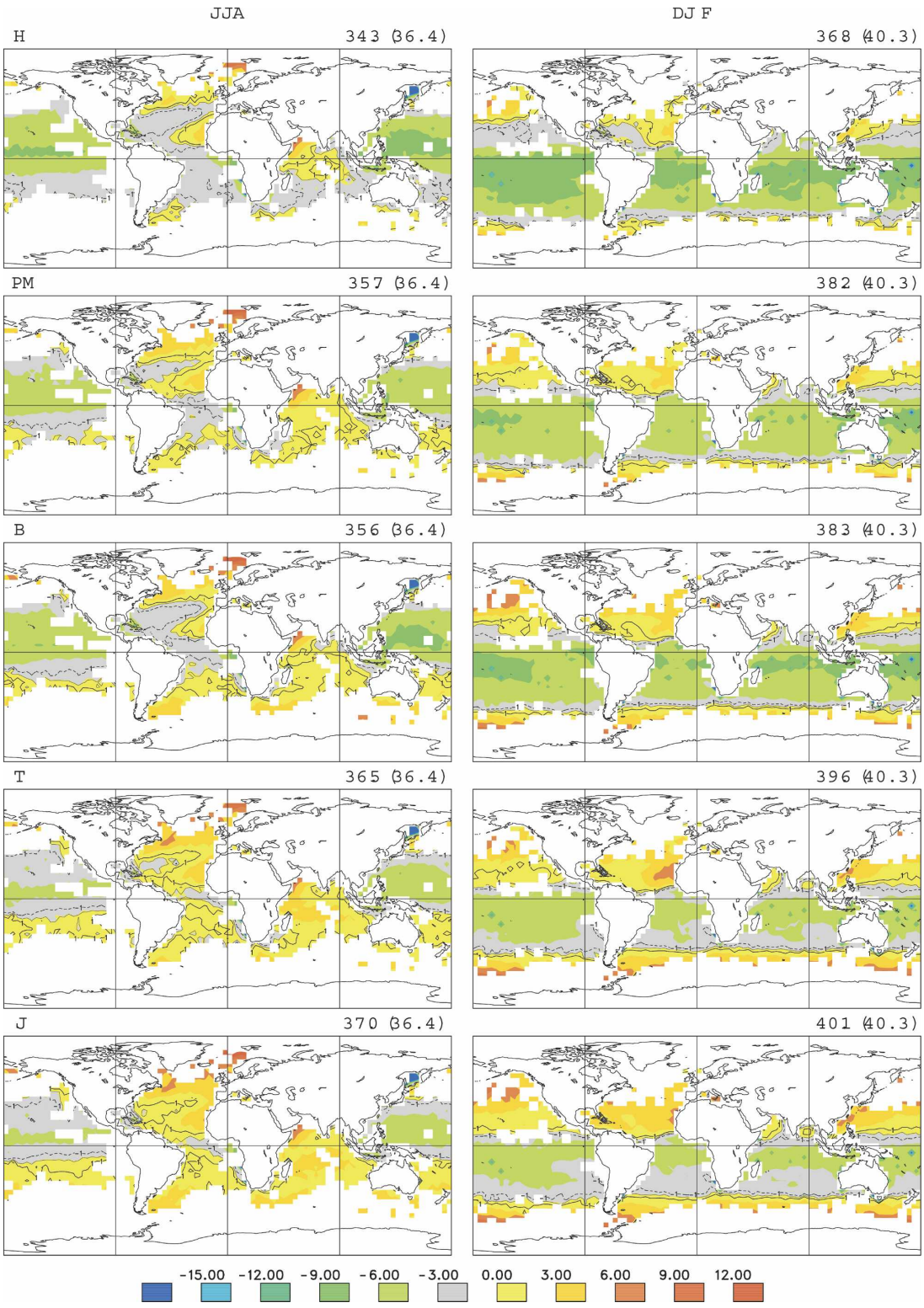

FIG. 13. Same as in Fig. 12, but GCM 5-yr mean upward solar flux (W m^{-2}) at TOA against the CERES data for the five OSA schemes. The numbers in bracket are the corresponding CERES results.

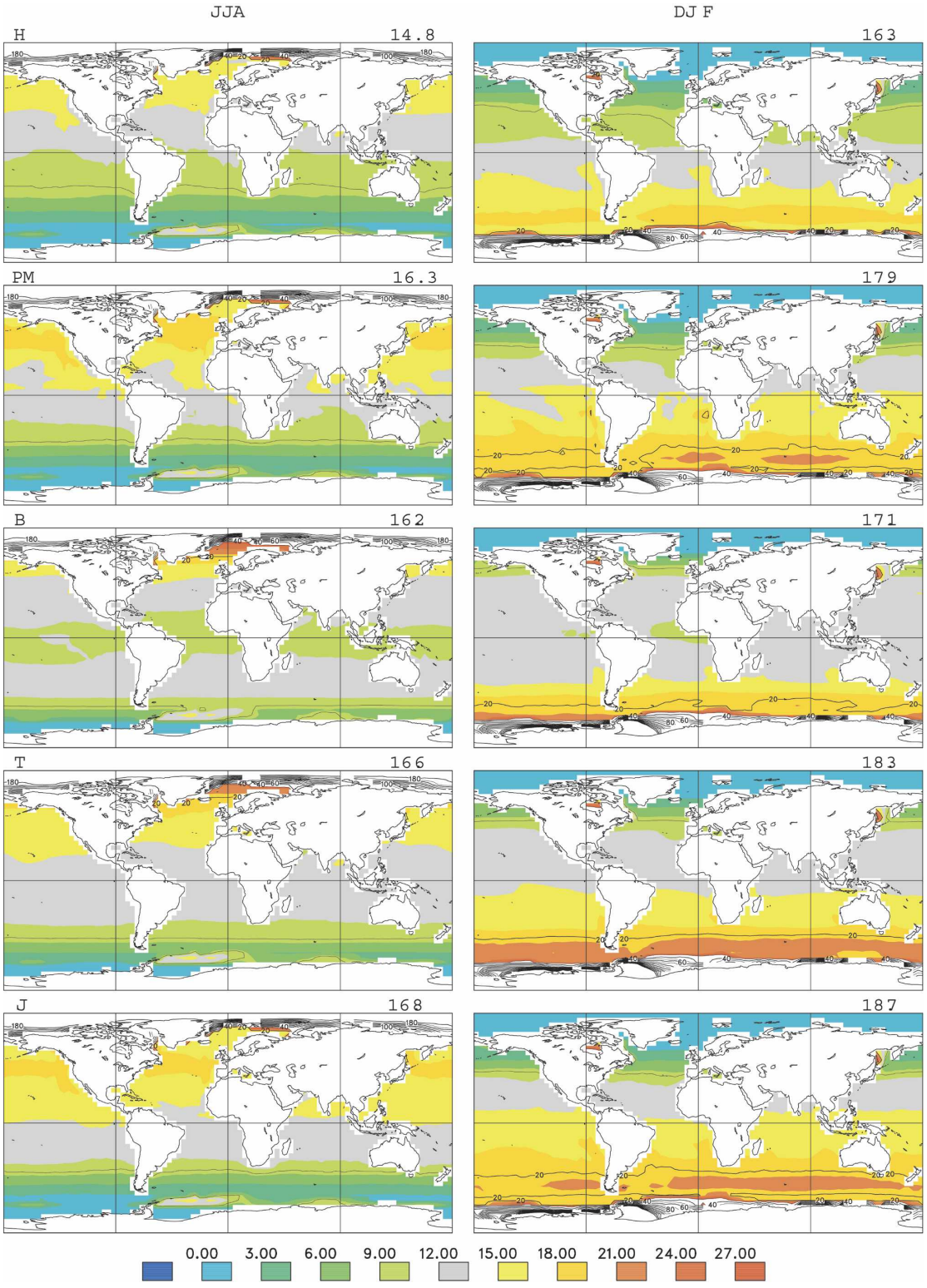

FIG. 14. Same as in Fig. 12, but for GCM 5-yr mean upward solar flux (W m^{-2}) at the surface for the five schemes.

and the OSA is an important issue for obtaining the accurate surface radiation budget. In this work a systematic comparison for several proposed OSA schemes are shown and the OSA impact on clear-sky radiation flux at the surface and TOA is studied by using a one-dimensional radiative transfer model and fully interacting GCM simulations.

Different OSA schemes depend on a variety of input factors. The solar zenith angle is the one input factor that is common in all schemes. The next most common input factor is the wind speed. The wind speed tends to become more important for large solar zenith angles. According to the J scheme, the role of wind speed becomes less important as the aerosol/cloud optical depth increases. Of the H, PM, and J schemes, the H and PM schemes display the most sensitivity to wind speed.

While all schemes are based on theory or observations, the clear-sky differences between schemes can be significant. For example, both the B and T schemes depend solely on solar zenith angle, but their OSA can differ by as much as 50%.

The one-dimensional radiative transfer model revealed that the reflected clear-sky upward fluxes at TOA corresponding to different OSA schemes could also be very different from each other with differences of up to 20 W m^{-2}. Analysis indicated that the T scheme had a unique SZA dependence of upward flux relative to the other schemes. The T scheme displayed a monotonically increasing flux for decreasing SZA. This feature of the T scheme prevents it from obtaining the correct instantaneous radiation results. The one-dimensional radiative transfer model was also used to calculate daily averaged results for the clear-sky upward flux. This indicated similarity between several of the schemes and was found to be helpful in understanding the results from the GCM simulations.

For the J scheme, the OSA is spectrally dependent. Figure 6 shows that the OSA spectral dependence changes as solar zenith angle changes. The one-dimensional radiative transfer model results indicate that although the total radiation flux could be similar, the energy distribution in different bands could be different between the broadband and the spectral band OSA scheme. The difference is up to 5 W m^{-2} in upward flux for the visible band. This could have impact on the chemical process that is dependent on certain specified ranges.

The GCM 5-yr-averaged results for clear-sky radiation are generally consistent with the one-dimensional radiation model results. For example, in JJA the OSA of the B scheme is lower in the Tropics and the northern extratropics but higher in the southern extratropics in comparison with the T scheme. The response of the GCM simulations has reduced the differences between schemes relative to the offline calculations. In the GCM results the different OSA schemes produce differences of only a few watts per meters squared in the upward flux at TOA. It is interesting that the T and J schemes are found to have very similar TOA upward fluxes given that their OSA dependence on SZA and wind speed appears to be so different (Fig. 4). This similarity was found to result from a cancellation of positive and negative differences between the schemes when averaged over the diurnal cycle.

Given some significant differences in the clear-sky upward fluxes, global energy balance at the TOA and at the surface (dependent on all-sky conditions) is remarkably insensitive to the use of any of the albedo formulations. This indicates the importance of the cloud forcing relative to clear-sky forcing in the calculation of these budgets.

Comparisons of the GCM response to the recent CERES data indicate that most of OSA schemes produces reasonable upward flux at TOA with a bias in the global mean of less than ± 2.5 W m^{-2}. Among them, the J, PM, and T schemes most closely match the CERES data. Comparison of the GCM response against ERBE data reveal a large and consistent negative bias in upward clear-sky flux.

The present study has considered the GCM response to differing OSA schemes only for the case of prescribed sea surface temperatures and sea ice extent. Future work will involve a similar investigation in which the response of a coupled atmosphere–ocean GCM will be considered for the different OSA formulations.

Acknowledgments. The authors thank Drs. H. Barker, T. Charlock, and Z. Jin and for helpful discussions, three anonymous reviewers for helpful comments, and D. Roberge for help with some of the calculations.

APPENDIX A

Analytical Formula for the PM Scheme

PM86 is a scheme using the ray-tracing method based on Fresnel reflection on the ocean surface. The OSA of the PM scheme is parameterized as follows. First a reference wind speed, W_o, is defined in terms of zenith angle as

$$W_o = 180\mu_o^3(1 - \mu_o^2).$$

Then when the wind speed $W_s \geq W_o$ the direct component is given as

$$A_{\text{dir}}(\mu_o, W_s) = 0.021 + 0.0421(1 - \mu_o)^2 + 0.128(1 - \mu_o)^3 - 0.04(1 - \mu_o)^6 + \left[\frac{4}{5.68 + W_s - W_o} + \frac{0.074(1 - \mu_o)}{1 + 3(W_s - W_o)}\right](1 - \mu_o)^6, \quad \text{(A1)}$$

and when $W_s < W_o$ the direct component is given as

$$A_{\text{dir}}(\mu_o, W_s) = \left[1. + \frac{5.4\mu_o^2(1 - \mu_o^2)W_s(W_s - 1.1W_o)^2}{W_o^3}\right]\left\{0.021 + 0.0421(1 - \mu_o)^2 + 0.128(1 - \mu_o)^3 - 0.04(1 - \mu_o)^6 + \left[\frac{4}{5.68} + 0.074(1 - \mu_o)\right](1 - \mu_o)^6\right\}. \quad \text{(A2)}$$

In either case the diffuse component is given as

$$A_{\text{dif}}(W_s) = 0.022\left\{1 + 0.55\exp\left[-\left(\frac{W_s}{7}\right)^2\right] + 1.45\exp\left[-\left(\frac{W_s}{40}\right)^2\right]\right\}. \quad \text{(A3)}$$

The final albedo value is a linear combination of the direct and diffuse components:

$$A = f_{\text{dir}}A_{\text{dir}} + f_{\text{dif}}A_{\text{dif}},$$
$$f_{\text{dir}} = \frac{F_{\text{dir}}}{F_{\text{dir}} + F_{\text{dif}}},$$
$$f_{\text{dif}} = 1 - f_{\text{dir}}. \quad \text{(A4)}$$

Here F_{dir} and F_{dif} are local values of the direct and diffuse surface flux.

In GCM simulations, the white cap effect (Monahan and MacNiocaill 1986) has been included as

$$A_{\text{total}} = A(1 - f) + 0.3f,$$

where A is the OSA and $f = 3.84 \times 10^{-06}W_s^{3.41}$ is the fractional weight of the white cap.

APPENDIX B

Daily Average for the 1D Model

We briefly discuss how to calculate the daily averaged results for different latitudes, since this has not been addressed in the one-dimensional radiative transfer study. This method provides a more realistic comparison to the results of GCM.

The solar zenith angle θ_0 is generally given by

$$\cos\theta_0 = \sin\delta\sin\phi + \cos\delta\cos\phi\cos\omega, \quad \text{(B1)}$$

where δ is declination angle, ϕ is the geographic latitude, and ω is hour angle with noon zero and morning positive. The declination angle is a function of day number (Iqbal 1983) as $\delta = f(\Gamma)$, where $\Gamma = 2\pi(d_n - 1)/365$, where d_n is the day number of the year, ranging from 1 on 1 January to 365 on 31 December.

At the sunrise moment $\theta_0 = \pi/2$. From (B1) $\omega_s = \cos^{-1}(-\tan\delta\tan\phi)$, which is the hour angle for the sunrise, thus $-\omega_s$ is the hour angle for the sunset. The integral of ω over $\pm\omega_s$ generates the daily averaged results. Note, if $\cos\omega_s > 1$ there is no sunrise (polar night); if $\cos\omega_s \leq -1$ there is no sunset and the solar zenith angle is given by (B1) with $\pi \geq \omega - \pi$.

REFERENCES

Barker, H. W., and Z. Li, 1995: Improved simulation of clear-sky shortwave radiative transfer in the CCC-GCM. *J. Climate,* **8,** 2213–2223.

Barkstrom, B. R., 1984: The Earth Radiation Budget Experiment (ERBE). *Bull. Amer. Meteor. Soc.,* **65,** 1170–1185.

Briegleb, B. P., P. Minnis, V. Ramanathan, and E. Harrison, 1986: Comparison of regional clear-sky albedos inferred from satellite observations and model computations. *J. Climate Appl. Meteor.,* **25,** 214–226.

Cox, C., and W. Munk, 1954: Measurement of roughness of the sea surface from photographs of the sun's glitter. *J. Opt. Soc. Amer.,* **44,** 838–850.

Dobbie, J. S., J. Li, R. Harvey, and P. Chylek, 2003: Sea-salt optical properties and GCM forcing at solar wavelengths. *Atmos. Res.,* **65,** 211–233.

Gleckler, P., 1996: *AMIP Newsletter.* No. 8, 24 pp. [Available online at http://www-pcmdi.llnl.gov/projects/amip/NEWS/.]

Hansen, J., G. Russell, D. Rind, P. Stone, A. Lacis, S. Lebedeff, R. Ruedy, and L. Travis, 1983: Efficient three-dimensional global models for climate studies: Models I and II. *Mon. Wea. Rev.,* **111,** 609–662.

Iqbal, M., 1983: *An Introduction to Solar Radiation.* Academic Press, 390 pp.

Jacobson, M. Z., 2001: Global direct radiative forcing due to multicomponent anthropogenic and natural aerosols. *J. Geophys. Res.,* **106,** 1551–1568.

Jin, Z., T. P. Charlock, and K. Rutledge, 2002: Analysis of broadband solar radiation and albedo over the ocean surface at COVE. *J. Atmos. Oceanic Technol.,* **19,** 1585–1601.

——, ——, W. L. Smith Jr., and K. Rutledge, 2004: A parameterization of ocean surface albedo. *Geophys. Res. Lett.,* **31,** L22301, doi:10.1029/2004GL021180.

Li, J., and Q. Min, 2002: Parameterization of the optical properties of sulfate aerosols in the infrared. *J. Atmos. Sci.,* **59,** 3130–3140.

——, and H. W. Barker, 2005: A radiation algorithm with correlated k-distribution. Part I: Local thermal equilibrium. *J. Atmos. Sci.,* **62,** 286–309.

——, J. G. Wong, J. S. Dobbie, and P. Chylek, 2001: Parameterization of the optical properties and growth of sulfate aerosols. *J. Atmos. Sci.,* **58,** 193–209.

Loeb, N. G., S. Kato, N. M. Smith, S. K. Gupta, W. F. Miller, P. Minnis, and B. A. Wielicki, 2003a: Angular distribution models for top-of-atmosphere radiative flux estimation from the Clouds and the Earth's Radiant Energy System instrument on the Tropical Rainfall Measuring Mission satellite. Part I: Methodology. *J. Appl. Meteor.,* **42,** 240–265.

——, K. Loukachine, N. M. Smith, S. P. Minnis, and B. A. Wielicki, 2003b: Angular distribution models for top-of-atmosphere radiative flux estimation from the Clouds and the Earth's Radiant Energy System instrument on the Tropical Rainfall Measuring Mission satellite. Part II: Validation. *J. Appl. Meteor.,* **42,** 1748–1769.

Lohmann, U., and E. Roeckner, 1996: Design and performance of a new cloud microphysics scheme developed for the ECHAM general circulation model. *Climate Dyn.,* **12,** 557–572.

McClatchey, R. A., R. W. Fenn, J. E. A. Selby, F. E. Volz, and J. S. Garing, 1972: Optical properties of the atmosphere. 3d ed. AFCRL-72-0497, 108 pp. [NTIS N7318412.]

McFarlane, N. A., G. J. Boer, J.-P. Blanchet, and M. Lazare, 1992: The Canadian Climate Centre second-generation general circulation model and its equilibrium climate. *J. Climate,* **5,** 1013–1044.

——, J. F. Scinocca, M. Lazare, R. Harvey, D. Verseghy, and J. Li, 2005: The CCCma third generation atmospheric general circulation model. CCCma Internal Rep., 25 pp. [Available online at http://www.cccma.ec.gc.ca/mode.]

Monahan, E. C., and G. MacNiocaill, 1986: *Oceanic Whitecaps and Their Role in Air-Sea Exchange Processes.* Reidel, 294 pp.

Payne, R. E., 1972: Albedo of the sea surface. *J. Atmos. Sci.,* **29,** 959–970.

Preisendorfer, R. W., and C. D. Mobley, 1986: Albedos and glitter patterns of a wind-roughened sea surface. *J. Phys. Oceanogr.,* **16,** 1293–1316.

von Salzen, K., and N. A. McFarlane, 2002: Parameterization of the bulk effects of lateral and cloud-top entrainment in transient shallow cumulus clouds. *J. Atmos. Sci.,* **59,** 1405–1429.

——, ——, and M. Lazare, 2005: The role of shallow convection in the water and energy cycles of the atmosphere. *Climate Dyn.,* **25,** 671–688.

Taylor, J. P., J. M. Edwards, M. D. Glew, P. Hignett, and A. Slingo, 1996: Studies with a flexible new radiation code. II: Comparisons with aircraft short-wave observations. *Quart. J. Roy. Meteor. Soc.,* **122,** 839–861.

Wielicki, B. A., and Coauthors, 1998: Clouds and the Earth's Radiant Energy System (CERES): Algorithm overview. *IEEE Trans. Geosci. Remote Sens.,* **36,** 1127–1141.